

# Ultra-high differential mobility and velocity of Néel walls in spin valves with planar-transverse polarizers under low perpendicularly injected currents

Mei Li,<sup>1</sup> Zhong An,<sup>2</sup> and Jie Lu<sup>2,\*</sup>

<sup>1</sup>Physics Department, Shijiazhuang University, Shijiazhuang, Hebei 050035, China

<sup>2</sup>College of Physics and Information Engineering, Hebei Advanced Thin Films Laboratory, Hebei Normal University, Shijiazhuang 050024, China

(Dated: April 23, 2019)

Transverse domain wall (TDW) dynamics in long and narrow spin valves with perpendicular current injection is theoretically investigated. We demonstrate that stable traveling-wave motion of TDWs with finite velocity survives for strong enough planar-transverse polarizers. For typical ferromagnetic materials (for example, Co) and achievable spin polarization ( $P = 0.6$ ), TDWs acquire a velocity over  $10^3$  m/s under a current density below  $10^7$  A/cm<sup>2</sup>. This efficiency is comparable with that of perpendicular polarizers. More importantly, in this case the wall has infinite “differential mobility” around the onset of stable wall excitation. Our results open new possibilities for developing magnetic nanodevices based on TDW propagation with low energy consumption. Also, analytics for parallel and perpendicular polarizers perfectly explains existing simulation findings. Finally, further boosting of TDWs by external uniform transverse magnetic fields is investigated and turns out to be efficient.

## I. INTRODUCTION

Tremendous progress in fabrication technology of non-volatile magnetic nanodevices has led to a great revolution in modern information industry[1–3]. In these nanodevices, magnetic domains with different orientations build zeros and ones in binary world. Intermediate regions separating these domains are the domain walls (DWs) and their motion leads to the data transformation[4–8]. Generally, DWs’ motion can be induced by magnetic fields, spin-polarized currents or temperature gradient, etc. Among them, the current-induced case is the easiest to implement in real experiments.

Historically, the earliest current-induced driving mechanism of DWs is the spin-transfer torque (STT). It was first calculated in a magnetic multilayer, in which two ferromagnetic (FM) layers are single-domained with “current perpendicular to the plane (CPP)” configuration[9]. The resultant STT is the so-called Slonczewski torque (SLT) and proportional to  $\mathbf{m} \times (\mathbf{m} \times \mathbf{m}_p)$  in which  $\mathbf{m}$  and  $\mathbf{m}_p$  are normalized magnetization vectors in the thin (free) and thick (pinned) layers. Meantime, another torque ( $\propto \mathbf{m} \times \mathbf{m}_p$ ) also exists and is usually referred as the field-like torque (FLT) since now  $\mathbf{m}_p$  acts like an effective field. Later in magnetic nanostrips with currents flowing in strip plane (CIP), adiabatic and nonadiabatic STTs are proposed and can be viewed as the continuous limits of SLT and FLT, respectively[10, 11]. The adiabatic STT induces the initial DW movement but the final steady wall velocity is determined by the nonadiabatic STT. However, since the exchange interaction avoids abrupt variation of magnetization, CIP current densities of several  $10^8$  A/cm<sup>2</sup> only induce DW velocity around 100 m/s.

To increase current efficiency, long and narrow spin valves (LNSVs) or magnetic tunneling junctions (MTJs) with CPP configuration are proposed to be host systems[12–14]. In these multilayers, DWs in free layers are driven to move along the long axis by spin-polarized current filtered by pinned layers (polarizers). Early simulations on parallel and perpendic-

ular polarizers only considered SLTs and asserted that the current efficiency can not be increased too much[15, 16]. In 2009, a significant breakthrough[17] was made by Khvalkovskiy *et al.* in which numerical simulations with both SLT and FLT reveal that to achieve a DW velocity of 100 m/s, the CPP current density for parallel polarizers is lowered to  $10^7$  A/cm<sup>2</sup>, while for perpendicular polarizers, the CPP current density is further decreased to  $10^6$  A/cm<sup>2</sup>.

Later, two series of experimental works were carried out. First, in LNSVs[18] and half-ring MTJs[19–21] with CPP configuration, transport measurements confirm that DWs can propagate with velocities as high as 500-800 m/s at current density below  $10^7$  A/cm<sup>2</sup>. Second, in ZigZag LNSVs with CIP configuration high DW velocities (150-600 m/s) are obtained for current densities of  $(2 \sim 5) \times 10^7$  A/cm<sup>2</sup> by using photoemission electron microscopy combined with X-ray magnetic circular dichroism[22–25]. Vertical spin current coming with spin flux transformation from pinned layers to free layers via spacers (thus similar to CPP) is suggested to provide a potential explanation for this velocity boosting.

Except for these concentrated explorations on parallel and perpendicular polarizers, LNSVs with planar-transverse polarizers have not received enough attention in existing literatures. In this work, within a mature Lagrangian framework[26] we show that stable traveling-wave motion of DWs with finite velocity exists for strong enough planar-transverse polarizers. The resulting current efficiency is comparable with that of perpendicular polarizers. More interestingly, an infinite “differential mobility” emerges around the onset of stable wall excitation. Also, we provide analytics for parallel and perpendicular polarizers which perfectly explains existing simulations. At last, further boosting of DWs by uniform transverse magnetic fields (UTMFs) are studied with the help of one-dimensional asymptotic expansion method (1D-AEM)[27–31].

## II. MODEL AND METHOD

We consider a LNSV with CPP configuration (see Fig. 1), which is composed of three layers: a free FM layer with tunable magnetization texture, a nonmagnetic (NM) metallic spacer and a pinned FM layer with a fixed magnetization orientation (polarizer). The global Cartesian coordinate system is as follows:  $\mathbf{e}_z$  is along the long axis of LNSV,  $\mathbf{e}_y$  follows the electron flow direction (from pinned to free layer) and  $\mathbf{e}_x = \mathbf{e}_y \times \mathbf{e}_z$ . The polarizer is usually made of hard ferromagnetic materials. Its magnetization ( $\mathbf{m}_p$ ) has three typical choices: (a)  $\mathbf{m}_p = \mathbf{m}_z$  (parallel), (b)  $\mathbf{m}_p = \mathbf{m}_y$  (perpendicular) and (c)  $\mathbf{m}_p = \mathbf{m}_x$  (planar-transverse). Electrons flow from the polarizer to the free layer via the metallic spacer with density  $J_e(>0)$ . Thus the charge current is  $J_{\text{charge}} = -J_e \mathbf{m}_y$ .

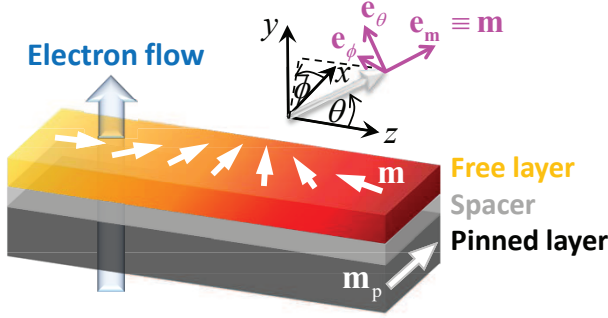


FIG. 1. (Color online) Sketch of a LNSV with CPP configuration, which is a three-layer structure: a pinned FM layer ( $\mathbf{m}_p$ , polarizer), a NM metallic spacer and a free FM layer ( $\mathbf{m}$ ). A DW in the free layer is driven to move along the long axis of LNSV by perpendicularly injected currents. ( $\mathbf{e}_x, \mathbf{e}_y, \mathbf{e}_z$ ) is the global Cartesian coordinate system, and ( $\mathbf{e}_m, \mathbf{e}_\theta, \mathbf{e}_\phi$ ) forms the local spherical coordinate system associated with  $\mathbf{m}$ .

The normalized magnetization  $\mathbf{m}$  of the free layer can be fully described by its polar angle  $\theta$  and azimuthal angle  $\phi$ . The associated local spherical coordinate system is denoted as ( $\mathbf{e}_m, \mathbf{e}_\theta, \mathbf{e}_\phi$ ). Then  $\mathbf{m}_p$  is decomposed into

$$\mathbf{m}_p = p_m \mathbf{e}_m + p_\theta \mathbf{e}_\theta + p_\phi \mathbf{e}_\phi, \quad (1)$$

with

$$\begin{aligned} p_m &= \sin \theta_p \cos(\phi - \phi_p) \sin \theta + \cos \theta_p \cos \theta, \\ p_\theta &= \sin \theta_p \cos(\phi - \phi_p) \cos \theta - \cos \theta_p \sin \theta, \\ p_\phi &= -\sin \theta_p \sin(\phi - \phi_p), \end{aligned} \quad (2)$$

where  $\theta_p$  ( $\phi_p$ ) is the polar (azimuthal) angle of  $\mathbf{m}_p$ .

The magnetic energy of the free layer includes the exchange, crystalline anisotropy, magnetostatic and FLT-induced effective potential. Following He's work[26], we have

$$\mathcal{E}[\mathbf{m}] = \mathcal{E}_0[\mathbf{m}] - \mu_0 M_s^2 \xi_{\text{CPP}} \frac{J_e b_p}{J_p c_p} \ln(1 + c_p p_m), \quad (3)$$

with

$$\mathcal{E}_0[\mathbf{m}] = J \left( \frac{\partial \mathbf{m}}{\partial z} \right)^2 + \mu_0 M_s^2 \left( -\frac{1}{2} k_E m_z^2 + \frac{1}{2} k_H m_y^2 \right), \quad (4)$$

in which the magnetostatic energy has been described by local quadratic terms of  $M_{x,y,z}$  by means of three average demagnetization factors[29].  $J$  is the exchange stiffness,  $\mu_0$  is the vacuum permeability,  $\xi_{\text{CPP}}$  describes the relative strength of FLT over SLT,  $k_E(k_H)$  is the total anisotropy coefficient along the easy (hard) axis of the free layer and  $M_s$  is the saturation magnetization. In addition,  $J_p \equiv 2\mu_0 e d M_s^2 / \hbar$  where  $d$  is the thickness of free layer,  $e(>0)$  is the absolute charge of electron and  $P$  is the spin polarization of the current. At last, the two dimensionless parameters  $b_p = 4P^{3/2}/3(1+P)^3 - 16P^{3/2}$  and  $c_p = (1+P)^3/[3(1+P)^3 - 16P^{3/2}]$  reproduce Slonczewski's original spin polarization factor  $g \equiv [-4 + (1+P)^3(3 + \mathbf{m} \cdot \mathbf{m}_p)/(4P^{3/2})]^{-1}$ [9] by  $g = b_p/(1 + c_p p_m)$ .

The magnetization dynamics in the free layer is described by the Lagrangian  $L = \int \mathcal{L} d^3 \mathbf{r}$  with density

$$\mathcal{L} = \frac{\mu_0 M_s}{\gamma_0} \dot{\phi} \cdot (1 - \cos \theta) - \mathcal{E}, \quad (5)$$

in which  $\gamma_0 = \mu_0 \gamma$  with  $\gamma$  being the gyromagnetic ratio and a dot means  $\partial/\partial t$ . To include the Gilbert damping and the SLT-induced anti-damping processes, an extra dissipation functional  $F = \int \mathcal{F} d^3 \mathbf{r}$  is introduced with density

$$\frac{\mathcal{F}}{\mu_0 M_s^2} = \frac{\alpha}{2} \frac{\dot{\theta}^2 + \dot{\phi}^2 \sin^2 \theta}{\gamma_0 M_s} - g \frac{J_e}{J_p} (p_\theta \sin \theta \dot{\phi} - p_\phi \dot{\theta}). \quad (6)$$

The corresponding generalized Euler-Lagrangian equation

$$\frac{d}{dt} \left( \frac{\delta \mathcal{L}}{\delta \dot{X}} \right) - \frac{\delta \mathcal{L}}{\delta X} + \frac{\delta \mathcal{F}}{\delta \dot{X}} = 0, \quad (7)$$

provides dynamical descriptions of TDWs, where  $X$  represents related collective coordinates.

Early simulations confirmed that in FM nanostrips with small enough cross section, transverse DWs (TDWs) have the lowest energy among all meta-stable states[32, 33]. In 2012, further simulations revealed that the stability range of TDW in free layers of LNSVs can be shifted towards larger cross section compared with monolayer strips, due to a magnetostatic screening effect between the free and pinned layers[34]. Therefore the configuration space of DWs in this work is the TDW with generalized Walker profile[35]

$$\ln \tan \frac{\vartheta(z, t)}{2} = \eta \frac{z - q(t)}{\Delta(t)}, \quad \phi(z, t) \equiv \varphi(t), \quad (8)$$

in which  $\eta = +1$  or  $-1$  represents head-to-head (HH) or tail-to-tail (TT) TDWs, respectively. Note that in many 1D collective-coordinate analysis, the tilting angle  $\varphi(t)$  and wall center position  $q(t)$  [or wall velocity  $\dot{q}(t)$ ] are the two collective coordinates meanwhile assuming fixed wall width  $\Delta(t)$ [36, 37]. However, the wall width does change considerably as the wall tilting angle varies if the material is magnetically biaxial. Even for uniaxial materials, the strip geometry will induce an effective hard axis in the normal direction perpendicular to strip plane. Based on these facts, we therefore view the wall width as the third collective coordinate.

In Eq. (7), by letting  $X$  take  $q(t)$ ,  $\varphi(t)$ ,  $\Delta(t)$  successively, and integrating over the long axis (i.e.  $\int_{-\infty}^{+\infty} dz$ ), we obtain the following dynamic equations

$$\frac{\dot{\varphi} + \alpha \eta \dot{q} / \Delta}{\gamma_0 M_s} = b_p \frac{J_e}{J_p} \left[ p_\varphi U(\varphi) - \frac{\xi_{\text{CPP}}}{2c_p} \ln \frac{1 - c_p \cos \theta_p}{1 + c_p \cos \theta_p} \right], \quad (9a)$$

$$\frac{\alpha \dot{\varphi} - \eta \dot{q} / \Delta}{\gamma_0 M_s} = b_p \frac{J_e}{J_p} \left[ \xi_{\text{CPP}} p_\varphi U(\varphi) + \frac{1}{2c_p} \ln \frac{1 - c_p \cos \theta_p}{1 + c_p \cos \theta_p} \right] - k_H \sin \varphi \cos \varphi, \quad (9b)$$

$$\frac{\pi^2 \alpha}{6 \gamma_0 M_s} \frac{\dot{\Delta}}{\Delta} = b_p \frac{J_e}{J_p} \left[ \xi_{\text{CPP}} W(\varphi) - p_\varphi U(\varphi) \ln \frac{1 - c_p \cos \theta_p}{1 + c_p \cos \theta_p} \right] + \left( \frac{l_0^2}{\Delta^2} - k_E - k_H \sin^2 \varphi \right). \quad (9c)$$

with

$$\begin{aligned} U(\varphi) &\equiv \chi / \sqrt{1 - c_p^2 [\sin^2 \theta_p \cos^2(\varphi - \phi_p) + \cos^2 \theta_p]}, \\ W(\varphi) &\equiv \frac{1}{2c_p} \left[ \frac{\pi^2}{4} + \frac{1}{4} \ln^2 \frac{1 - c_p \cos \theta_p}{1 + c_p \cos \theta_p} - \chi^2 \right], \\ \chi &\equiv \arccos \frac{c_p \sin \theta_p \cos(\varphi - \phi_p)}{\sqrt{1 - c_p^2 \cos^2 \theta_p}}, \end{aligned} \quad (10)$$

and  $l_0 \equiv \sqrt{2J/(\mu_0 M_s^2)}$  being the exchange length of the free layer. Note that in the definition of function  $W(\varphi)$  in Eq. (10), our calculation supports an additional “1/2” factor compared with He’s original work.

### III. DW DYNAMICS UNDER PLANAR-TRANSVERSE POLARIZERS

For planar-transverse polarizers,  $\theta_p = \pi/2$  and  $\phi_p = 0$ . The dynamical equations evolve to

$$\frac{1 + \alpha^2}{\gamma_0 M_s \sin \varphi} \frac{\eta \dot{q}}{\Delta} = \left[ k_H \cos \varphi - (\alpha - \xi_{\text{CPP}}) b_p \frac{J_e}{J_p} \tilde{U}(\varphi) \right], \quad (11a)$$

$$\frac{1 + \alpha^2}{\gamma_0 M_s \sin \varphi} \dot{\varphi} = - \left[ (1 + \alpha \xi_{\text{CPP}}) b_p \frac{J_e}{J_p} \tilde{U}(\varphi) + \alpha k_H \cos \varphi \right], \quad (11b)$$

$$\frac{\pi^2 \alpha}{6 \gamma_0 M_s} \frac{\dot{\Delta}}{\Delta} = \left( \frac{l_0^2}{\Delta^2} - k_E - k_H \sin^2 \varphi \right) + \xi_{\text{CPP}} b_p \frac{J_e}{J_p} \tilde{W}(\varphi), \quad (11c)$$

in which

$$\begin{aligned} \tilde{U}(\varphi) &= \frac{\tilde{\chi}}{\sqrt{1 - c_p^2 \cos^2 \varphi}}, \quad \tilde{W}(\varphi) = \frac{1}{2c_p} \left( \frac{\pi^2}{4} - \tilde{\chi}^2 \right), \\ \tilde{\chi} &= \arccos(c_p \cos \varphi). \end{aligned} \quad (12)$$

For steady traveling-wave mode,  $\dot{\varphi} = 0$  and  $\dot{\Delta} = 0$ . This

leads to two branches of solution:

$$\begin{aligned} \varphi_0 &= n\pi, \quad v_0 = 0, \\ \Delta(\varphi_0) &= l_0 \left[ k_E - \xi_{\text{CPP}} b_p \frac{J_e}{J_p} \tilde{W}(\varphi_0) \right]^{-1/2}, \end{aligned} \quad (13)$$

and

$$\begin{aligned} \cos \varphi'_0 &= - \frac{1 + \alpha \xi_{\text{CPP}}}{\alpha k_H} b_p \frac{J_e}{J_p} \tilde{U}(\varphi'_0), \\ v'_0 &= \frac{\eta \Delta(\varphi'_0) \gamma_0 k_H M_s}{1 + \alpha \xi_{\text{CPP}}} \sin \varphi'_0 \cos \varphi'_0, \\ \Delta(\varphi'_0) &= l_0 \left[ k_E + k_H \sin^2 \varphi'_0 - \xi_{\text{CPP}} b_p \frac{J_e}{J_p} \tilde{W}(\varphi'_0) \right]^{-1/2}. \end{aligned} \quad (14)$$

For the first branch in Eq. (13), For the variation  $\varphi = \varphi_0 + \delta\varphi$ , Eq. (11b) provides

$$\begin{aligned} \frac{\partial(\ln \delta\varphi)}{\partial t} &= - \frac{\gamma_0 M_s}{1 + \alpha^2} \left\{ (-1)^n (1 + \alpha \xi_{\text{CPP}}) b_p \frac{J_e}{J_p} \times \right. \\ &\quad \left. (1 - c_p^2)^{-1/2} \arccos[(-1)^n c_p] + \alpha k_H \right\}. \end{aligned} \quad (15)$$

The stability of  $\varphi_0$ -solution requires the terms in curly braces to be positive. This leads to  $J_e/J_p > j_d$  ( $n$  is even) or  $J_e/J_p < j_u$  ( $n$  is odd), where

$$\begin{aligned} j_u &\equiv \frac{\alpha k_H}{1 + \alpha \xi_{\text{CPP}}} \cdot \frac{\sqrt{1 - c_p^2}}{b_p \arccos(-c_p)}, \\ j_d &\equiv - \frac{\alpha k_H}{1 + \alpha \xi_{\text{CPP}}} \cdot \frac{\sqrt{1 - c_p^2}}{b_p \arccos(c_p)}. \end{aligned} \quad (16)$$

For the wall width of this branch, first its existence demands that when  $n$  is even (odd),  $J_e/J_p < j_{\Delta u}$  ( $J_e/J_p > j_{\Delta d}$ ) with

$$\begin{aligned} j_{\Delta u} &\equiv \frac{k_E}{\xi_{\text{CPP}}} \cdot \frac{2c_p}{b_p} \cdot \left( \frac{\pi^2}{4} - \arccos^2 c_p \right)^{-1}, \\ j_{\Delta d} &\equiv - \frac{k_E}{\xi_{\text{CPP}}} \cdot \frac{2c_p}{b_p} \cdot \left[ \arccos^2(-c_p) - \frac{\pi^2}{4} \right]^{-1}. \end{aligned} \quad (17)$$

Since  $\alpha \ll 1$  and  $\xi_{\text{CPP}} \ll 1$ ,  $|j_{\Delta u(d)}| \gg |j_{u(d)}|$  and is usually out of experimental accessibility. Thus only  $j_{u(d)}$  is considered when dealing with stability issue. For the variation  $\Delta = \Delta(\varphi_0) + \delta\Delta$ , Eq. (11c) provides

$$\frac{\pi^2 \alpha}{6 \gamma_0 M_s} \frac{\partial(\ln \delta\Delta)}{\partial t} = - \frac{2l_0^2}{\Delta^2(\varphi_0)}, \quad (18)$$

implying a stable wall width of this solution branch (see violet solid lines in Fig. 2).

Next we turn to the branch in Eq. (14). By rewriting the first equation as  $J_e/J_p = -\alpha k_H \cos \varphi'_0 (1 - c_p^2 \cos^2 \varphi'_0)^{1/2} / [(1 + \alpha \xi_{\text{CPP}}) b_p \arccos(c_p \cos \varphi'_0)]$  and analyzing its monotonicity,

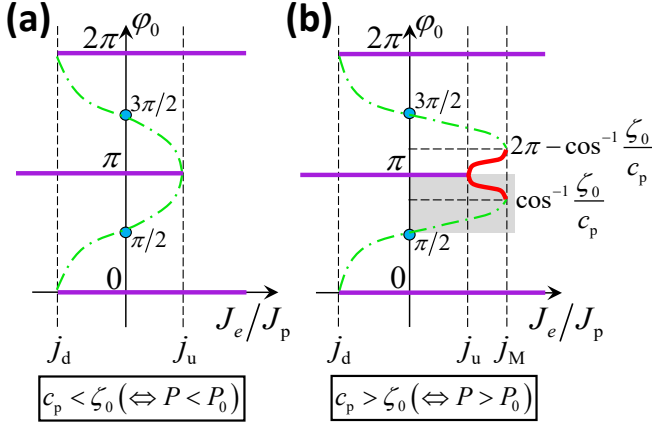


FIG. 2. (Color online) Illustration of the solution branch in Eq. (14): (a)  $c_p < \zeta_0$ , (b)  $c_p > \zeta_0$ . In both cases, violet solid lines represent the stable solution branch in Eq. (13) with zero velocity, and green dash-dot curves represent the unstable part of solution branch in Eq. (14). In addition, red solid curves in (b) indicate the stable part of solution branch in Eq. (14). The shaded area in (b) will be calculated in details in Fig. 3.

the permitted current density range of this branch can be obtained. Note that  $J_e(\phi'_0) = J_e(2\pi - \phi'_0)$ , we then focus on  $\phi'_0 \in [0, \pi]$  thus  $\sin \phi'_0 \geq 0$ . After standard calculus, one has

$$\frac{d}{d\phi'_0} \left( \frac{J_e}{J_p} \right) = \frac{\alpha k_H \sin \phi'_0}{(1 + \alpha \xi_{\text{CPP}}) b_p} \cdot \frac{f(\zeta)}{\sqrt{1 - \zeta^2} \cdot \arccos^2 \zeta}, \quad (19)$$

with

$$f(\zeta) = (1 - 2\zeta^2) \arccos \zeta + \zeta \sqrt{1 - \zeta^2}, \quad \zeta \equiv c_p \cos \phi'_0. \quad (20)$$

On the other hand, the counterpart of Eq. (15) for this solution branch is

$$\frac{\partial(\ln \delta \phi')}{\partial t} = \frac{\alpha \gamma_0 M_s k_H \sin^2 \phi'_0}{(1 + \alpha^2)(1 - \zeta^2) \arccos \zeta} f(\zeta), \quad (21)$$

The monotonicity analysis on  $f(\zeta)$  provides us a critical value  $\zeta_0 = -0.6256$  ( $\Leftrightarrow P_0 = 0.3704$ )[26]. When  $c_p < \zeta_0$  ( $\Leftrightarrow P < P_0$ ),  $f(\zeta) > 0$ . This fact has two consequences: from Eq. (19),  $J_e/J_p$  is an increasing function on  $\phi'_0 \in [0, \pi]$  thus acquires its minimum ( $j_d$ ) at  $\phi'_0 = 0$  and maximum ( $j_u$ ) at  $\phi'_0 = \pi$  (see Fig. 2(a)). However, Eq. (21) tells us that now this whole branch remains unstable thus is not physically preferred. When  $c_p > \zeta_0$  ( $\Leftrightarrow P > P_0$ ),  $f(\zeta)$  first increases when  $\phi'_0$  runs from 0 to  $\arccos(\zeta_0/c_p)$  and then decreases when  $\phi'_0$  exceeds  $\arccos(\zeta_0/c_p)$  to  $\pi$ . Correspondingly,  $J_e/J_p$  increases from  $j_d$  to  $j_M = 0.2172 \alpha k_H / [(1 + \alpha \xi_{\text{CPP}}) b_p c_p]$  and then decreases to  $j_u$ , as illustrated in Fig. 2(b). Meantime, from Eq. (21) only when  $\arccos(\zeta_0/c_p) < \phi'_0 < 2\pi - \arccos(\zeta_0/c_p)$  the solution branch in Eq. (14) is stable, which has been marked by red curves in Fig. 2(b).

Now we explain what happens physically when the CPP current density  $J_e$  increases from 0 to large positive value. If the wall initially lies in easy  $xz$ -plane with  $\phi|_{t=0} = 0$ , i.e. the

magnetization at wall center is parallel to the polarizer, then it always stays in this state with zero velocity no matter how large  $J_e$  is. While if the wall initially lies with  $\phi|_{t=0} = \pi$ , i.e. the magnetization at wall center is anti-parallel to the polarizer, it keeps on staying in this state until  $J_e/J_p$  increases to  $j_u$ . When  $J_e$  is further enhanced a little bit, something interesting happens. When the polarizer is not strong enough ( $P < P_0$ ), the wall “jumps” to  $\phi = 0$  state (through  $\pi \rightarrow 0$  or  $\pi \rightarrow 2\pi$  route depending on the nature of external disturbances) and then keeps still. On the contrary, if the polarizer is strong enough ( $P_0 < P \leq 1$ ), the wall will evolve into one of the two stable parts of the solution branch in Eq. (14). Likely, which one it runs into is determined by the nature of external disturbances. As  $J_e/J_p$  increases from  $j_u$  to  $j_M$ , the wall acquires a finite velocity as shown by the second equation of Eq. (14). When  $J_e/J_p$  exceeds  $j_M$ , the wall jumps to its nearest static branch under external disturbance and then keeps in this state.

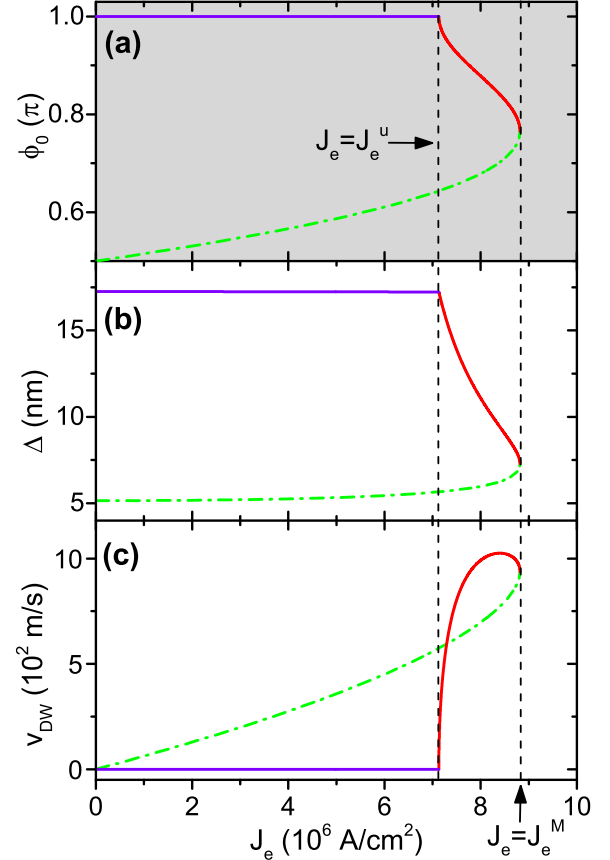


FIG. 3. (Color online) Dependence of the tilting angle (a), width (b) and velocity (c) of a TDW on current density in a LNSV with CPP configuration and planar-transverse polarizer ( $\mathbf{m}_p = \mathbf{e}_x$ ). The subfigure (a) corresponds to the shaded area in Fig. 2(b). The free FM layer has the geometry of  $50 \times 3 \times 8000 \text{ nm}^3$ , with  $M_s = 1400 \text{ kA/m}$ ,  $J = 30 \times 10^{-12} \text{ J/m}$  and  $\alpha = 0.007$ . In addition,  $P = 0.6$  and  $\xi_{\text{CPP}} = 0.1$  for spin-transfer process. The violet solid lines are those from the stable static branch in Eq. (13). The red solid (green dash-dot) curves comes from the stable (unstable) part of the finite-velocity branch in Eq. (14).



Next we do some numerical estimations. The following magnetic parameters for Co are adopted (same as those in Ref. [17]):  $M_s = 1400$  kA/m,  $J = 30 \times 10^{-12}$  J/m,  $\alpha = 0.007$  and  $\xi_{\text{CPP}} = 0.1$ . Thus the exchange length  $l_0 = 4.94$  nm. The geometry of free layer is  $3 \times 50 \times 8000$  nm<sup>3</sup>, resulting in three average demagnetization factors:  $D_y = 0.917251$ ,  $D_x = 0.082269$  and  $D_z = 0.000480$ . The crystalline anisotropy and edge roughness are both neglected, thus  $k_E = D_x - D_z = 0.081789$  and  $k_H = D_y - D_x = 0.834982$ . Then  $\Delta_0 = l_0/\sqrt{k_E} = 17.3$  nm. As indicated, to obtain stable propagating walls the spin polarization  $P$  should satisfy  $P > P_0 = 0.3704$ . Here we take  $P = 0.6$  as an example. Then  $b_p = 0.3832$  and  $b_p = 0.8442$ , thus the extremal point is  $\varphi_0^M = \arccos(\xi_0/c_p) = 0.7657\pi$ . The upper limit of the current density for the stable static branch in Eq. (13) is  $J_e^u = j_u \cdot J_p = 7.13 \times 10^6$  A/cm<sup>2</sup>. Meantime, the upper limit of the current density for the stable finite-velocity branch in Eq. (14) is  $J_e^M = j_M \cdot J_p = 8.82 \times 10^6$  A/cm<sup>2</sup>. These two values are both not high for real applications. Then the tilting angle, width and velocity of a TT ( $\eta = -1$ ) TDW corresponding to the shaded area in Fig. 2(b) are calculated and plotted in Fig. 3. We focus on the red curves which are the stable part of the finite-velocity branch in Eq. (14). Interestingly, at  $J_e \approx 8.40 \times 10^6$  A/cm<sup>2</sup> the wall can propagate along the LNSV at a velocity as high as 1025 m/s. Therefore planar-transverse polarizers have comparable current efficiency as perpendicular polarizers[17]. To our knowledge, this has never been reported before in existing studies.

Another attracting quantity is the “infinite differential mobility” ( $dv/dJ_e$ ) around  $J_e = J_e^u$  ( $\varphi'_0 = \pi$ ), as shown by the red curve in Fig. 3(c). From Eq. (19), this infinity comes from the divergent behavior of  $|d\varphi'_0/dJ_e| \propto 1/|\sin \varphi'_0| \rightarrow +\infty$  at  $J_e = J_e^u$  ( $\varphi'_0 = \pi$ ). Consequently, combining with Eq. (14), we have  $|dv'_0/dJ_e| = |(dv'_0/d\varphi'_0) \cdot (d\varphi'_0/dJ_e)| \propto |\cos 2\varphi'_0/\sin \varphi'_0| \rightarrow +\infty$ . This means that a slight increase of  $J_e$  above  $J_e^u$  will lead to considerable increase of wall velocity.

In summary, dynamical behaviors of TDWs under planar-transverse polarizers in LNSVs with CPP configuration are quite different from known results in two aspects. First, in all well-investigated current-driven stack setups, including FM monolayers (CIP), FM/heavy-metal bilayers (CIP) and LNSVs with parallel and perpendicular polarizers (CPP), TDWs have a finite mobility in the entire range of current density when dealing with a sufficiently smooth and even sample (absence of intrinsic pinning due to imperfectness). This means TDWs will acquire a steady motion with finite velocity under finite charge current density, no matter how small the latter is. However in LNSVs with strong enough planar-transverse polarizers, steady wall motion with finite velocity can only occur when driving current exceeds a finite threshold of density. Second, at the onset of wall excitation, the differential mobility is divergent due to the sudden change in steady tilting angle of TDWs as current density exceeds its lower limit a little bit. This allows TDWs to acquire high velocities under small current densities. The resulting current efficiency is comparable with that of perpendicular polarizers. When the

current density exceeds its upper limit, TDWs jump to their nearest static branch. These two exotic behaviors should open new possibilities for developing magnetic nanodevices based on TDW propagation with low energy consumption.

### III. DW DYNAMICS UNDER PARALLEL AND PERPENDICULAR POLARIZERS

The simulation work by Khvalkovskiy *et al.* proposed the high current efficiency in LNSVs under parallel and perpendicular polarizers with “ $\mathbf{m} \cdot \mathbf{m}_p$ -independent” STT coefficients[17]. Except for numerics, they also provided a 1D analysis for parallel polarizers in which the wall velocity and tilting angle are two collective coordinates. However, for perpendicular polarizers the corresponding 1D analysis is absent. Meantime, their simulations revealed that under perpendicular (parallel) polarizers pure SLT (FLT) induces persistent wall displacement while pure FLT (SLT) does not. Therefore they conjectured that at low currents the large difference for the wall velocities between perpendicular and planar polarizers is related to the factor  $\xi_{\text{CPP}}$  between the torques. However, the exact ratio of mobilities for these two cases under low currents is not provided. In this section, we perform systematic Lagrangian analysis and provide answers to these issues.

#### III.A Modified Lagrangian and dynamical equations

For  $\mathbf{m} \cdot \mathbf{m}_p$ -independent STT coefficients, the energy density functional turns to

$$\tilde{\mathcal{E}}[\mathbf{m}] = \mathcal{E}_0[\mathbf{m}] - \mu_0 M_s b_J p_{\mathbf{m}}, \quad (22)$$

and the dissipation functional becomes

$$\frac{\tilde{\mathcal{F}}}{\mu_0 M_s^2} = \frac{\alpha}{2} \frac{\dot{\theta}^2 + \dot{\phi}^2 \sin^2 \theta}{\gamma_0 M_s} - \frac{a_J}{M_s} (p_\theta \sin \theta \dot{\phi} - p_\phi \dot{\theta}), \quad (23)$$

where  $a_J = \hbar J_e P / (2\mu_0 d e M_s)$  and  $b_J = \xi_{\text{CPP}} a_J$ . Still, the generalized Walker profile is taken as the configuration space of walls. After putting the wall center position  $q(t)$ , tilting angle  $\varphi(t)$  and width  $\Delta(t)$  into Eq. (7) successively, and integrating over  $z \in (-\infty, +\infty)$ , a new set of dynamical equations are obtained

$$\alpha \eta \frac{\dot{q}}{\Delta} + \dot{\phi} = \gamma_0 \left( \frac{\pi}{2} a_J p_\varphi + b_J \cos \theta_p \right), \quad (24a)$$

$$\eta \frac{\dot{q}}{\Delta} - \alpha \dot{\phi} = \gamma_0 M_s k_H \sin \varphi \cos \varphi + \gamma_0 \left( a_J \cos \theta_p - \frac{\pi}{2} b_J p_\varphi \right), \quad (24b)$$

$$\frac{\pi^2 \alpha}{6} \frac{\dot{\Delta}}{\Delta} = \gamma_0 M_s \left( \frac{l_0^2}{\Delta^2} - k_E - k_H \sin^2 \varphi \right) + \gamma_0 \pi b_J \sin \theta_p \cos(\varphi - \phi_p). \quad (24c)$$

### III.B Parallel polarizers

For systematicness, we first briefly revisit TDW dynamics under parallel polarizers. In this case,  $\mathbf{m}_p = \mathbf{m}_z$ , thus  $\theta_p = 0$  and then  $p_\varphi = 0$ . The dynamical equations turn to

$$\frac{1 + \alpha^2}{\gamma_0} \frac{\eta \dot{\varphi}}{\Delta} = \frac{k_H M_s}{2} \sin 2\varphi + (a_J + \alpha b_J), \quad (25a)$$

$$\frac{1 + \alpha^2}{\gamma_0} \dot{\varphi} = -\frac{\alpha k_H M_s}{2} \sin 2\varphi + (b_J - \alpha a_J), \quad (25b)$$

$$\frac{\pi^2 \alpha}{6\gamma_0 M_s} \frac{\dot{\Delta}}{\Delta} = \frac{l_0^2}{\Delta^2} - k_E - k_H \sin^2 \varphi. \quad (25c)$$

The first two equations reproduce Eq. (4) in Khvalkovskiy's work (see Ref. [17]) and the third one provides the TDW width. For traveling-wave mode of TDW,  $\dot{\varphi} = 0$  and  $\dot{\Delta} = 0$ . This leads to a FLT-determined steady wall velocity

$$\begin{aligned} v_0 &= \frac{\eta \Delta(\varphi_0) \gamma_0 \xi_{\text{CPP}} a_J}{\alpha}, \\ \sin 2\varphi_0 &= \frac{2(\xi_{\text{CPP}} - \alpha) a_J}{\alpha M_s k_H}, \\ \Delta_1(\varphi_0) &= l_0 (k_E + k_H \sin^2 \varphi_0)^{-1/2}. \end{aligned} \quad (26)$$

For variation of  $\varphi_0$ , we have

$$\frac{\partial(\ln \delta \varphi_0)}{\partial t} = -\frac{\alpha \gamma_0 M_s k_H \cos 2\varphi_0}{2(1 + \alpha^2)}. \quad (27)$$

When  $\cos 2\varphi_0 > 0$ , i.e.  $|\varphi_0 - n\pi| < \pi/4$ , the  $\varphi_0$ -solution is stable. On the other hand, for variation of  $\Delta_1$ , one has

$$\frac{\pi^2 \alpha}{6\gamma_0 M_s} \frac{\partial(\delta \Delta)}{\partial t} = -\frac{2l_0^2}{\Delta_1^3(\varphi_0)} \delta \Delta - \Delta_1(\varphi_0) k_H \sin 2\varphi_0 \delta \varphi_0. \quad (28)$$

Thus the wall width should be stable as long as  $\varphi_0$  is stable.

Next we compare our analytics with existing simulation data. The geometry and magnetic parameters of the free layer are the same as those in the end of Sec. II, except that the spin polarization is changed to  $P = 0.32$  (same as in Khvalkovskiy's work). By requiring  $|\sin 2\varphi_0| \leq 1$ , the Walker limit (under which traveling-wave mode survives) is  $J_W = \alpha M_s k_H / (2\kappa |\xi_{\text{CPP}} - \alpha|) = 2.20 \times 10^8 \text{ A/cm}^2$ . However this is just theoretical prediction based on the generalized Walker profile. Real simulations (see Fig. 1(b) of Ref. [17]) revealed that TDWs disappear due to global-spin-transfer-induced domain excitation when  $J_e > 2.4 \times 10^7 \text{ A/cm}^2$  which is an order of magnitude smaller  $J_W$ . Thus in traveling-wave mode, at most  $\sin^2 \varphi_0 \sim 10^{-2}$  and  $\Delta_1(\varphi_0) \sim \Delta_0 = 17.3 \text{ nm}$ . This leads to a constant wall mobility  $\sim 1.09 \times 10^{-5} \text{ (m/s)/(A/cm}^2\text{)}$ , which perfectly explains the linear dependence of wall velocity on current density in Fig. 1(b) of Ref. [17]. In Fig. 2 of our work, analytical results from Eq. (26) are plotted by solid curves. Meantime, numerical data from Fig. 1(b) in Ref. [17] are indicated by solid squares. Obviously as long as TDWs exist ( $J_e < 2.4 \times 10^7 \text{ A/cm}^2$ ), our theoretical results are in good agreement with numerical simulations.

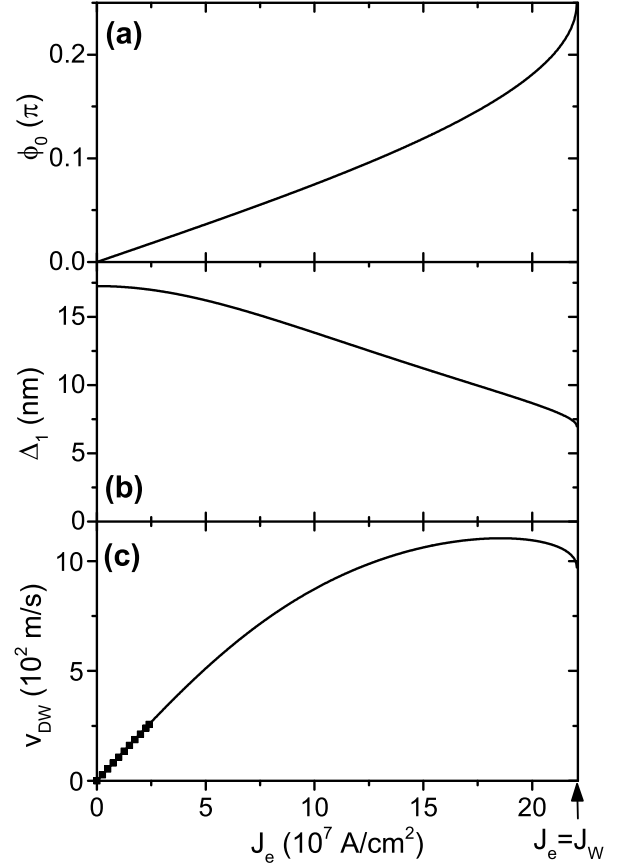


FIG. 4. Dependence of the tilting angle (a), width (b) and velocity (c) of a TDW on current density in a LNSV with CPP configuration and parallel polarizer ( $\mathbf{m}_p = \mathbf{e}_z$ ). The geometry and magnetic parameters of the free layer are the same as those in Fig. 3, except that the spin polarization is changed to  $P = 0.32$ . The solid curves are from Eq. (26) and the solid squares in (c) are from Fig. 1(b) in Ref. [17] with exactly the same geometric and magnetic parameters.

### III.C Perpendicular polarizers

Now  $\mathbf{m}_p = \mathbf{m}_y$ , thus  $\theta_p = \pi/2$  and  $\phi_p = \pi/2$ . Then  $p_\varphi = \cos \varphi$  and Eq. (24) is simplified to

$$\frac{1 + \alpha^2}{\gamma_0} \frac{\eta \dot{\varphi}}{\Delta} = \left[ k_H M_s \sin \varphi + \frac{\pi}{2} (\alpha a_J - b_J) \right] \cos \varphi, \quad (29a)$$

$$\frac{1 + \alpha^2}{\gamma_0} \dot{\varphi} = \left[ \frac{\pi}{2} (a_J + \alpha b_J) - \alpha k_H M_s \sin \varphi \right] \cos \varphi, \quad (29b)$$

$$\frac{\pi^2 \alpha}{6\gamma_0 M_s} \frac{\dot{\Delta}}{\Delta} = \left( \frac{l_0^2}{\Delta^2} - k_E - k_H \sin^2 \varphi \right) + \frac{\pi b_J}{M_s} \sin \varphi. \quad (29c)$$

For steady traveling-wave mode, we need  $\dot{\varphi} = 0$  and  $\dot{\Delta} = 0$ . This leads to two branches of solution:

$$\begin{aligned} \varphi_0 &= \left(n + \frac{1}{2}\right) \pi, \quad v_0 = 0, \\ \Delta_2(\varphi_0) &= l_0 \left[ k_E + k_H - (-1)^n \frac{\pi b_J}{M_s} \right]^{-1/2}, \end{aligned} \quad (30)$$

and

$$\begin{aligned}\sin \phi'_0 &= \frac{\pi}{2} \frac{1 + \alpha \xi_{\text{CPP}}}{\alpha} \frac{a_J}{k_H M_s}, \\ v'_0 &= \frac{\pi}{2} \frac{\eta \Delta_2(\phi'_0) \gamma_0 a_J}{\alpha} \cos \phi'_0, \\ \Delta_2(\phi'_0) &= l_0 \left( k_E + k_H \sin^2 \phi'_0 - \frac{\pi b_J}{M_s} \sin \phi'_0 \right)^{-1/2}.\end{aligned}\quad (31)$$

Then we perform stability analysis to these two branches. For the one in Eq. (30), after taking variation of  $\phi_0$  and substituting it into Eq. (29b), one has

$$\frac{\partial(\ln \delta \phi_0)}{\partial t} = -\frac{\alpha \gamma_0 M_s k_H}{1 + \alpha^2} \left[ \frac{\pi}{2} \left( \frac{1}{\alpha} + \xi_{\text{CPP}} \right) \frac{(-1)^n a_J}{k_H M_s} - 1 \right]. \quad (32)$$

Then we define  $J_1 \equiv 4|\xi_{\text{CPP}} - \alpha| \pi^{-1} (1 + \alpha \xi_{\text{CPP}})^{-1} J_W$ . When  $J_e > J_1$  ( $n$  is even) or  $J_e < -J_1$  ( $n$  is odd),  $(-1)^n (\alpha^{-1} + \xi_{\text{CPP}}) a_J \pi / (2 k_H M_s) - 1 > 0$  always holds thus the  $\phi_0 = (n + 1/2)\pi$  solution in the first branch is stable. For the wall width of this branch, similar variational analysis provides the same result as in Eq. (18), implying that the static solution at  $\phi_0 = (n + 1/2)\pi$  always has a stable wall width.

Then we move to the other branch in Eq. (31). The solution  $\phi'_0$  requires  $|\sin \phi'_0| \leq 1$ , which is equivalent to  $|J_e| \leq J_1$ . After varying  $\phi'_0$  by  $\delta \phi'$  and putting into Eq. (29b), we have

$$\frac{\partial(\ln \delta \phi')}{\partial t} = -\frac{\alpha \gamma_0 M_s k_H \cos^2 \phi'_0}{1 + \alpha^2}, \quad (33)$$

implying that  $\phi'_0$ -solution is always stable. The corresponding TDW velocity can be explicitly written out as

$$v'_0 = \frac{\pi}{2} \frac{\eta \Delta_2(\phi'_0) \gamma_0 a_J}{\alpha} (-1)^m \sqrt{1 - \left( \frac{\pi}{2} \frac{1 + \alpha \xi_{\text{CPP}}}{\alpha k_H M_s} a_J \right)^2}, \quad (34)$$

in which “ $(-1)^m$ ” comes from the initial condition  $(\phi'_0|_{t=0} = m\pi \text{ at } t = 0)$ . For  $|J_e| \ll J_1$ , one has

$$v'_0 \approx \frac{\pi}{2} \frac{\eta \Delta_0 \gamma_0 a_J}{\alpha} (-1)^m. \quad (35)$$

Clearly it has a mobility larger than that of “parallel-polarizer” case [see Eq. (26)] by a factor of  $\pi/(2\xi_{\text{CPP}}) \approx 15.7$ , thus well explains the higher current efficiency of perpendicular polarizers. When  $|J_e| \rightarrow J_1$ , the  $\phi'_0$ -solution converges to  $\phi_0$ -branch with zero wall velocity.

For the same magnetic parameters as in parallel polarizers,  $J_1 = 0.1183 J_W = 2.61 \times 10^7 \text{ A/cm}^2$ . For HH TDWs ( $\eta = +1$ ) and standard initial condition  $(\phi_0|_{t=0} = \phi'_0|_{t=0} = 0)$ , the solution branch in Eq. (30) [Eq. (31)] is plotted in Fig. 3 by solid line (curve) in shaded (white-background) area. In addition, simulation data from Fig. 2(b) in Ref. [17] are depicted in our Fig. 3(c) by solid squares. Clearly when  $J_e \leq 0.3 \times 10^7 \text{ A/cm}^2$ , our analytics coincides with simulation data very well. For larger current density, the wall configuration in simulations will be distorted from the standard Walker profile due to global spin transfers, thus leads to the inconsistency between analytics and simulations.

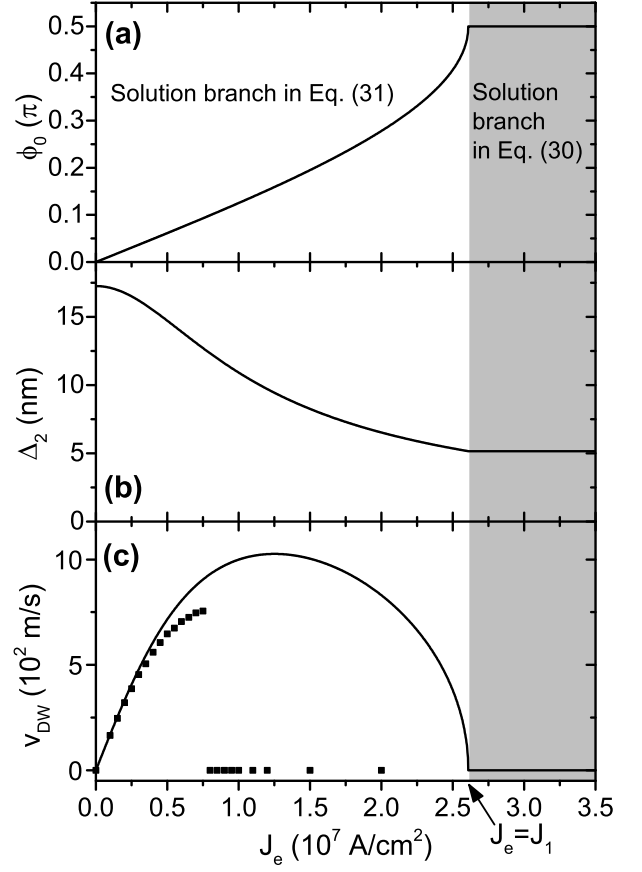


FIG. 5. Dependence of the tilting angle (a), width (b) and velocity (c) of a TDW on current density in a LNSV with CPP configuration and perpendicular polarizer ( $\mathbf{m}_p = \mathbf{e}_y$ ). The geometry and magnetic parameters of the free layer are the same as those in Fig. 4. The solid curves in the white-background area are the solution branch in Eq. (31) and the solid lines in the shaded area are those from Eq. (30). The solid squares in (c) are from Fig. 2(b) in Ref. [17].

### III.D Comparison with experimental data

As mentioned in Sec. I, to our knowledge there are two groups of experimental work. In the first group, currents with definite density inject perpendicularly into LNSVs or half-ring MTJs (genuine CPP configurations). While in the second group, in-plane current flows through ZigZag LNSVs and the vertical spin current is suggested to be the source of DW velocity boosting, however the corresponding spin current density is hard to estimate. Therefore we focus on the first group in which genuine CPP configuration with definite current density is under investigation. Furthermore, our analytics is obtained in a strip geometry (resulting in three averaged demagnetization factors, and hence  $k_E$  and  $k_H$ ), thus can not directly apply to half-ring geometry. In summary, the best case to make the comparison is the first case in the first group, which is the experimental work by Boone *et al.* in 2010[18] on LNSVs with parallel polarizers.

In their work, the free layer is made of Permalloy (Py) with  $M_s = 430$  kA/m and the crystalline anisotropy is neglected. Its geometry ( $3 \times 90 \times 5000$  nm<sup>3</sup>) provides three average demagnetization factors:  $D_y = 0.9473$ ,  $D_x = 0.05182$  and  $D_z = 0.00088$ . Thus we have  $k_E = D_x - D_z = 0.0509$  and  $k_H = D_y - D_x = 0.8955$ . The resulting coercive force is  $k_E M_s = 275$  Oe, which is consistent with experimental measurements (Py reversal at +200 and -300 Oe) in Fig. 2(b) of Ref. [18]. The exchange stiffness ( $J$ ) has not been explicitly provided. However from the fixed wall width ( $\lambda = 53$  nm) they adopted in simulations, we have  $J = \mu_0 k_E M_s^2 \lambda^2 / 2 = 16.6 \times 10^{-12}$  J/m. Furthermore, the conversion coefficient from current density to SLT strength is  $\kappa = a_J / J_e = \hbar P / (2 \mu_0 d e M_s) = 1.32 \times 10^{-3}$  (A/m)/(A/cm<sup>2</sup>) for  $P = 0.65$ . Now we estimate the wall mobility under small driving currents where the wall width can be viewed as constant ( $\lambda = 53$  nm). Note that they obtained a damping coefficient from a fitting to the rectified voltage with zero-FLT assumption. However as indicated by Khvalkovskiy *et al.*, FLT is crucial for TDW dynamics in LNSVs with parallel polarizers. Therefore we adopt the typical Py value  $\alpha = 0.01$  rather than their fitting parameter. Moreover, we assume  $\xi_{\text{CPP}} = 0.1$  which is the maximum permissible in Ref. [18]. From Eq. (26), the wall mobility is  $|v_0 / J_e| = \lambda \gamma_0 \xi_{\text{CPP}} \kappa / \alpha = 1.55 \times 10^{-4}$  (m/s)/(A/cm<sup>2</sup>). This agrees well with their experimental data for  $J_e < 2 \times 10^6$  A/cm<sup>2</sup> in their Fig. 4(b). On the other hand, the fitting result  $\alpha = 0.09$  leads to a wall mobility of  $1.72 \times 10^{-5}$  (m/s)/(A/cm<sup>2</sup>). This is an order of magnitude smaller than the experimental observations thus should be abandoned.

#### IV. FURTHER BOOSTING BY UTMFS

In real magnetic nondevices composed of LNSVs, to further boost TDWs' propagation, a UTMF

$$\mathbf{H}_{\text{TMF}} = H_{\perp} (\cos \Phi_{\perp}, \sin \Phi_{\perp}, 0) \quad (36)$$

can be applied, with  $H_{\perp}$  and  $\Phi_{\perp}$  being the UTMF strength and orientation, respectively. However, rigorous profile and velocity of TDWs under an arbitrary UTMF are hard to obtain due to the mismatch between symmetries in different energy terms in transverse direction. Since we focus on the traveling-mode at low current density, the 1D-AEM on dynamical equation shall provide useful information[27–31]. By putting Eqs. (22) and (23) into the generalized Euler-Lagrangian equation (7) with  $X = \theta(\phi)$ , we obtain the familiar Landau-Lifshitz-Gilbert (LLG) equation

$$\begin{aligned} \frac{\partial \mathbf{m}}{\partial t} = & -\gamma_0 \mathbf{m} \times \mathbf{H}_{\text{eff}} + \alpha \mathbf{m} \times \frac{\partial \mathbf{m}}{\partial t} \\ & - \gamma_0 a_J \mathbf{m} \times (\mathbf{m} \times \mathbf{m}_p) - \gamma_0 b_J \mathbf{m} \times \mathbf{m}_p, \end{aligned} \quad (37)$$

with the effective field  $\mathbf{H}_{\text{eff}} = -(\mu_0 M_s)^{-1} \delta \mathcal{E}_0 / \delta \mathbf{m}$ . This is the platform where 1D-AEM applies.

$\mathbf{H}_{\text{TMF}}$  is then appended to  $\mathbf{H}_{\text{eff}}$  for further study. Meanwhile, the pinned layer is assumed to be unaffected by

UTMFs, which is a harmless simplification and will not affect our main conclusion. Recalling the results in Sec. II, for TDWs moving under planar-transverse polarizers, 1D-AEM is not applicable since stable wall motion with finite velocity can only be excited for current density exceeding a finite threshold. Hence in this section, we present the results for parallel and perpendicular polarizers.

#### IV.A Parallel polarizers

The 1D-AEM needs static profiles of TDWs as the basis to calculate the response of the system under external stimuli. Depending on UTMF strength, static TDWs take different profiles. Therefore we discuss the “small UTMF” and “finite UTMF” cases separately.

For small UTMFs, the CCP current density, UTMF, and inverse of time are rescaled simultaneously, that is  $a_J = \varepsilon a_J^0$ ,  $b_J = \varepsilon b_J^0$ ,  $H_{\perp} = \varepsilon h_{\perp}$  and  $1/t = \varepsilon(1/\tau)$ , where  $\varepsilon$  is the rescaling infinitesimal. The real solution of the LLG equation is expanded as  $\Omega(z, t) = \Omega_0(z, \tau) + \varepsilon \Omega_1(z, \tau) + O(\varepsilon^2)$  with  $\Omega = \theta, \phi$ . Putting them back into the original LLG equation (37), the solution to the zeroth-order equation is the Walker ansatz. At the first order of  $\varepsilon$ , with the help of zeroth-order solutions, the differential equation about  $\theta_1$  reads,

$$\begin{aligned} F_s = \mathcal{L} \theta_1, \quad \mathcal{L} & \equiv \frac{2J}{\mu_0 M_s} \left( -\frac{d^2}{dz^2} + \frac{\theta_0'''}{\theta_0'} \right), \\ F_s & \equiv \left[ \frac{\eta \alpha(z_0) \tau}{\gamma_0 \Delta_0} - b_J^0 \right] \sin \theta_0 + (-1)^n h_{\perp} \cos \theta_0 \cos \Phi_{\perp}, \end{aligned} \quad (38)$$

where  $(z_0)_{\tau} \equiv dz_0/d\tau$  and a prime means  $d/dz$ . The subscript “s” indicates the “small UTMF” case. Note that  $\mathcal{L}$  is the same 1D self-adjoint Schrödinger operator as given in Refs. [27–31]. Following the “Fredholm alternative”, by demanding  $\theta_0'$  (kernel of  $\mathcal{L}$ ) to be orthogonal to the function  $F_s$  defined in Eq. (38), TDW velocity in traveling-wave mode under small UTMFs is

$$V_s = \varepsilon(z_0)_{\tau} = \eta \gamma_0 \Delta_0 b_J / \alpha, \quad (39)$$

which reproduces the rigorous result in Eq. (26).

For finite UTMFs, we rescale the current density and the TDW velocity ( $V_f$ ) simultaneously, i.e.  $a_J = \varepsilon a_J^0$ ,  $b_J = \varepsilon b_J^0$  and  $V_f = \varepsilon v$  in which the subscript “f” denotes the “finite UTMF” case. By introducing the traveling coordinate  $\tilde{z} \equiv z - V_f t = z - \varepsilon v t$ ,  $\theta(z, t)$  and  $\phi(z, t)$  are expanded as  $\Omega(z, t) = \Omega_0(\tilde{z}) + \varepsilon \Omega_1(\tilde{z}) + O(\varepsilon^2)$  with  $\Omega = \theta, \phi$ . Substituting them into the LLG equation, an approximate polar angle profile  $\theta_0$  (solution to the zeroth-order equations) of the wall is obtained

$$\ln \frac{\sin \theta_0 - \sin \theta_{\infty}}{1 + \cos(\theta_0 + \theta_{\infty})} = \frac{\eta \tilde{z}}{\Delta(\phi_{\infty}) / \cos \theta_{\infty}}, \quad (40)$$



with

$$\begin{aligned}\phi_\infty &= \tan^{-1} [k_E \tan \Phi_\perp / (k_E + k_H)], \\ \theta_\infty &= \sin^{-1} \frac{H_\perp}{M_s \sqrt{k_E^2 \cos^2 \phi_\infty + (k_E + k_H)^2 \sin^2 \phi_\infty}},\end{aligned}\quad (41)$$

$$\Delta(\phi_\infty) = l_0 (k_E + k_H \sin^2 \phi_\infty)^{-1/2},$$

in which  $\theta_\infty$  ( $\phi_\infty$ ) is the polar (azimuthal) angle of magnetization in domains. At the first order of  $\varepsilon$ , after similar process as in field-driven case[29], the equation about  $\theta_1$  is

$$\mathcal{L}(\theta_1) = F_f \equiv v\gamma_0^{-1}(\alpha\theta'_0 - \sin\theta_0\phi'_0) - b_J^0 \sin\theta_0. \quad (42)$$

where a “prime” means  $d/dz$ . Again,  $\theta'_0$  (kernel of  $\mathcal{L}$ ) should be orthogonal to the function  $F_f$ . After similar calculation, TDW velocity in traveling-wave mode under finite UTMF is,

$$\begin{aligned}V_f &= u(\theta_\infty) \frac{\eta\gamma_0\Delta(\phi_\infty)b_J}{\alpha}, \\ u(\theta_\infty) &= \frac{2\cos\theta_\infty}{2\cos\theta_\infty - (\pi - 2\theta_\infty)\sin\theta_\infty}.\end{aligned}\quad (43)$$

This clearly shows that UTMFs can boost TDW propagation by a factor  $u(\theta_\infty)$ , which has been well studied in Ref. [29].

#### IV.B Perpendicular polarizers

For small UTMFs, after similar rescaling, expansion and substitution operations, the differential equation about  $\theta_1$  is,

$$\mathcal{L}\theta_1 = \frac{\eta\alpha(z_0)\tau\sin\theta_0}{\gamma_0\Delta_0} + (-1)^n (h_\perp \cos\theta_0 \cos\Phi_\perp - a_J^0). \quad (44)$$

The corresponding wall velocity is,

$$V_s = \varepsilon(z_0)\tau = (-1)^n \eta\pi\gamma_0\Delta_0 a_J / (2\alpha), \quad (45)$$

which is the  $\phi'_0 \rightarrow n\pi$  limit of Eq. (31).

For finite UTMFs, the equation about  $\theta_1$  is

$$\mathcal{L}\theta_1 = \frac{v}{\gamma_0}(\alpha\theta'_0 - \sin\theta_0\phi'_0) - a_J^0 \cos\phi_0 + b_J^0 \cos\theta_0 \sin\phi_0. \quad (46)$$

The existence condition of  $\theta_1$ -solution provides

$$\begin{aligned}V_f &\approx \omega(\theta_\infty) \frac{\eta\gamma_0\Delta(\phi_\infty)a_J}{\alpha} \cos\phi_\infty, \\ \omega(\theta_\infty) &= \frac{\pi - 2\theta_\infty}{2\cos\theta_\infty - (\pi - 2\theta_\infty)\sin\theta_\infty}.\end{aligned}\quad (47)$$

Simple calculus shows that  $\omega(\theta_\infty)$  has similar divergent behavior as  $u(\theta_\infty)$  when  $H_\perp \rightarrow H_\perp^{\max}$ , thus considerably boost TDW motion. Interestingly, in LNSVs with perpendicular polarizers, TDW motion can be manipulated not only by UTMF strength (via “ $\omega(\theta_\infty)$ ”) but also its orientation (via “ $\cos\phi_\infty$ ”). This comes from the fact that polarized electrons always act as an extra time-dependent effective field in hard axis. For TDWs

with  $\phi_\infty \neq n\pi$ , magnetization in wall region rotates around the effective field hence results in a translational wall displacement along “ $\eta\mathbf{e}_z$ ” direction. Meanwhile, projection of SLT to the hard axis  $\mathbf{e}_y$  contributes to “ $\cos\phi_\infty$ ”. These lead to the final “ $\eta\cos\phi_\infty$ ” factor in Eq. (47).

#### VII. SUMMARY

In this work, TDW dynamics in LNSVs with CPP configurations are systematically investigated within Lagrangian framework. When STT coefficients take the Slonczewski’s original form, our results show that stable traveling-wave motion of TDWs with finite velocity can survive for strong enough planar-transverse polarizers, with the current efficiency comparable with that of perpendicular ones. More importantly, TDWs have infinite “differential mobility” around the onset of stable wall excitation. These results should provide insights for developing magnetic nanodevices with low energy consumption. For  $\mathbf{m} \cdot \mathbf{m}_p$ -independent STT coefficients, analytics for parallel and perpendicular polarizers perfectly explain existing simulations and experiments. At last, further boosting of TDWs by external UTMFs are investigated with help of 1D-AEM and turns out to be efficient.

#### ACKNOWLEDGEMENT

This work is supported by the National Natural Science Foundation of China (Grants No. 11374088). Z. An also acknowledges the support from the Hebei Province Department of Education (GCC2014025).

---

\* [jlu@hebtu.edu.cn](mailto:jlu@hebtu.edu.cn)

- [1] F. H. D. Leeuw, R. V. D. Doel, and U. Enz, Rep. Prog. Phys. **43**, 689 (1980).
- [2] Y. Tserkovnyak, A. Brataas, G. E. W. Bauer, and B. I. Halperin, Rev. Mod. Phys. **77**, 1375 (2005).
- [3] M. Kläui, J. Phys.: Condens. Matter **20**, 313001 (2008).
- [4] D. A. Allwood, G. Xiong, C. C. Faulkner, D. Atkinson, D. Petit, and R. P. Cowburn, Science, **309**, 1688 (2005).
- [5] M. Hayashi, L. Thomas, R. Moriya, C. Rettner, and S. S. P. Parkin, Science **320**, 209 (2008).
- [6] J. H. Franken, H. J. M. Swagten, and B. Koopmans, Nat. Nanotechnol. **7**, 499 (2012).
- [7] J. Münchenberger, G. Reiss, and A. Thomas, J. Appl. Phys. **111**, 07D303 (2012).
- [8] S. S. P. Parkin and S.-H. Yang, Nat. Nanotechnol. **10**, 195 (2015).
- [9] J. Slonczewski, J. Magn. Magn. Mater. **159**, L1 (1996).
- [10] Z. Li and S. Zhang, Phys. Rev. Lett. **92**, 207203 (2004).
- [11] G. Tatara, H. Kohno, and J. Shibata, Phys. Rep. **468**, 213 (2008).
- [12] J. Grollier, D. Lacour, V. Cros, A. Hamzic, A. Vaurès, and A. Fert, D. Adam and G. Faini, J. Appl. Phys. **92**, 4825 (2002).

- [13] J. Grollier, P. Boulenc, V. Cros, A. Hamzić, A. Vaurès, A. Fert, and G. Faini, *Appl. Phys. Lett.* **83**, 509 (2003).
- [14] C. K. Lim, T. Devolder, C. Chappert, J. Grollier, V. Cros, A. Vaurès, A. Fert, and G. Faini, *Appl. Phys. Lett.* **84**, 2820 (2004).
- [15] A. Rebei and O. Mryasov, *Phys. Rev. B* **74**, 014412 (2006).
- [16] K. Kawabata, M. Tanizawa, K. Ishikawa, Y. Inoue, M. Inuishi, and T. Nishimura, presented at the 2011 International Conference on Simulation of Semiconductor Processes and Devices, 2011 (unpublished).
- [17] A. V. Khvalkovskiy, K. A. Zvezdin, Ya. V. Gorbunov, V. Cros, J. Grollier, A. Fert, and A. K. Zvezdin, *Phys. Rev. Lett.* **102**, 067206 (2009).
- [18] C. T. Boone, J. A. Katine, M. Carey, J. R. Childress, X. Cheng, and I. N. Krivorotov, *Phys. Rev. Lett.* **104**, 097203 (2010).
- [19] A. Chanthbouala, R. Matsumoto, J. Grollier, V. Cros, A. Anane, A. Fert, A. V. Khvalkovskiy, K. A. Zvezdin, K. Nishimura, Y. Nagamine, H. Maehara, K. Tsunekawa, A. Fukushima, and S. Yuasa, *Nat. Phys.* **7**, 626 (2011).
- [20] P. J. Metaxas, J. Sampaio, A. Chanthbouala, R. Matsumoto, A. Anane, A. Fert, K. A. Zvezdin, K. Yakushiji, H. Kubota, A. Fukushima, S. Yuasa, K. Nishimura, Y. Nagamine, H. Maehara, K. Tsunekawa, V. Cros, and J. Grollier, *Sci. Rep.* **3**, 1829 (2013).
- [21] J. Sampaio, S. Lequeux, P. J. Metaxas, A. Chanthbouala, R. Matsumoto, K. Yakushiji, H. Kubota, A. Fukushima, S. Yuasa, K. Nishimura, Y. Nagamine, H. Maehara, K. Tsunekawa, V. Cros, and J. Grollier, *Appl. Phys. Lett.* **103**, 242415 (2013).
- [22] S. Pizzini, V. Uhlíř, J. Vogel, N. Rougemaille, S. Laribi, V. Cros, E. Jiménez, J. Camarero, C. Tieg, and E. Bonet, *Appl. Phys. Express* **2**, 023003 (2009).
- [23] V. Uhlíř, S. Pizzini, N. Rougemaille, J. Novotný, V. Cros, E. Jiménez, G. Faini, L. Heyne, F. Sirotti, C. Tieg, A. Bendounan, F. Maccherozzi, R. Belkhou, J. Grollier, A. Anane, and J. Vogel, *Phys. Rev. B* **81**, 224418 (2010).
- [24] V. Uhlíř, S. Pizzini, N. Rougemaille, V. Cros, E. Jiménez, L. Ranno, O. Fruchart, M. Urbánek, G. Gaudin, J. Camarero, C. Tieg, F. Sirotti, E. Wagner, and J. Vogel, *Phys. Rev. B* **83**, 020406(R) (2011).
- [25] V. Uhlíř, J. Vogel, N. Rougemaille, O. Fruchart, Z. Ishaque, V. Cros, J. Camarero, J. C. Cezar, F. Sirotti, and S. Pizzini, *J. Phys.: Condens. Matter* **24**, 024213 (2012).
- [26] P.-B. He, *Eur. Phys. J. B* **86**, 412 (2013).
- [27] A. Goussev, R. G. Lund, J. M. Robbins, V. Slastikov, and C. Sonnenberg, *Phys. Rev. B* **88**, 024425 (2013).
- [28] A. Goussev, R. G. Lund, J. M. Robbins, V. Slastikov, and C. Sonnenberg, *Proc. R. Soc. A* **469**, 20130308 (2013).
- [29] J. Lu, *Phys. Rev. B* **93**, 224406 (2016).
- [30] M. Li, J. B. Wang, and J. Lu, *Sci. Rep.* **7**, 43065 (2017).
- [31] M. Yu, M. Li, and J. Lu, *Nanomaterials* **9**, 128 (2019).
- [32] R. D. McMichael and M. J. Donahue, *IEEE Trans. Magn.* **33**, 4167 (1997).
- [33] Y. Nakatani, A. Thiaville, and J. Miltat, *J. Magn. Magn. Mater.* **290**, 750 (2005).
- [34] N. Rougemaille, V. Uhlíř, O. Fruchart, S. Pizzini, J. Vogel, and J. C. Toussaint, *Appl. Phys. Lett.* **100**, 172404 (2012).
- [35] N. L. Schryer and L. R. Walker, *J. Appl. Phys.* **45**, 5406 (1974).
- [36] C. T. Boone and I. N. Krivorotov, *Phys. Rev. Lett.* **104**, 167205 (2010).
- [37] J. Shibata, G. Tatara, and H. Kohno, *Journal of Physics D: Applied Physics* **44**, 384004 (2011).